


SCIENTIFIC REPORTS

OPEN

The Transition to Paschen's Law for Microscale Gas Breakdown at Subatmospheric Pressure

Amanda M. Loveless¹, Guodong Meng², Qi Ying², Feihong Wu², Kejing Wang², Yonghong Cheng² & Allen L. Garner^{1,3} 

Received: 7 January 2019

Accepted: 25 March 2019

Published online: 05 April 2019

The decrease in electronic device size necessitates greater understanding of gas breakdown and electron emission at microscale to optimize performance. While traditional breakdown theory using Paschen's law (PL), driven by Townsend avalanche, fails for gap distance $d \lesssim 15 \mu\text{m}$, recent studies have derived analytic equations for breakdown voltage when field emission and Townsend avalanche drive breakdown. This study derives a new analytic equation that predicts breakdown voltage V_B within 4% of the exact numerical results of a previously derived theory and new experimental results at subatmospheric pressure for gap distances from 1–25 μm . At atmospheric pressure, V_B transitions to PL near the product of pressure and gap distance, pd , corresponding to the Paschen minimum; at lower pressures, the transition to PL occurs to the left of the minimum. We further show that the work function plays a major role in determining which side of the Paschen minimum V_B transitions to PL as pressure approaches atmospheric pressure while field enhancement and the secondary emission coefficient play smaller roles. These results indicate that appropriate combinations of these parameters cause V_B to transition to PL to the left of the Paschen minimum, which would yield an extended plateau similar to some microscale gas breakdown experimental observations.

Gas breakdown in the presence of electric fields is desirable for generating microplasmas for combustion¹, electric propulsion², or medical and environmental applications^{3–7} and deleterious in accelerators⁸, fusion devices⁹, micro and nanoelectronics^{10,11}, and pulsed power biological experiments¹². All these scenarios require accurately predicting gas breakdown at microscale gaps or smaller; however, the standard theory for predicting gas breakdown voltage V_B given by Paschen's law (PL)¹³ fails because field emission (FE), rather than Townsend avalanche (TA), drives breakdown at these scales^{14,15}. Given by $V_B = B_p pd / [\ln(A_p pd) - \ln[\ln(1 + \gamma_{SE}^{-1})]]$, where p is the pressure, d is the gap distance, γ_{SE} is the secondary electron emission coefficient, and A_p and B_p are gas constants, PL¹³ is characterized by a minimum V_B that occurs when $pd = \exp(1)A_p^{-1} \ln(1 + \gamma_{SE}^{-1})$; however, at microscale, this minimum vanishes or is replaced by an extended plateau^{14,15}.

Several mathematical models and simulations^{15–23} have predicted V_B as a function of gap distance and/or pressure to demonstrate the transition to FE. Because many of these models must be solved numerically—and those that are analytic often do not fully incorporate all mechanisms to elucidate limiting behavior—more recent studies have applied matched asymptotic theory to analytically unify FE and TA for argon at atmospheric pressure²⁴, any gas at atmospheric pressure²⁵, and any gas at any pressure for FE or TA driven breakdown²⁶. These models can also quantify the relative contributions of FE and TA to breakdown^{25–27}, demonstrate the transitions between the mechanisms, and yield an analytic expression similar to traditional vacuum breakdown^{27,28}. More recent simulations have shown that electrodes with multiple sharp protrusions yielded an effective PL that combined the individual PL for each protrusion²⁹. While potentially contributing to the observed extended plateau, these simulations did not fully incorporate field emission. Furthermore, real electrodes, even when polished to control surface roughness, may not necessarily have distinct, well-defined, sharp tips.

Many (albeit not all) microscale gas breakdown experiments focus on breakdown at atmospheric pressure, which is critical for the aforementioned biomedical^{6,7}, environmental⁵, and combustion applications¹. However, gas breakdown plays a major role in limiting the power levels of high power microwave devices from 1 to

¹School of Nuclear Engineering, Purdue University, West Lafayette, Indiana, 47907, USA. ²State Key Laboratory of Electrical Insulation and Power Equipment, Xi'an Jiaotong University, Xi'an, 710049, China. ³School of Electrical and Computer Engineering, Purdue University, West Lafayette, Indiana, 47907, USA. Correspondence and requests for materials should be addressed to G.M. (email: gdmengxjtu@xjtu.edu.cn) or A.L.G. (email: algarner@purdue.edu)

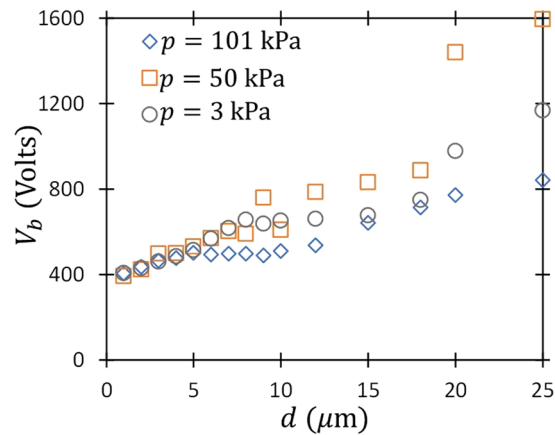


Figure 1. Measured breakdown voltage (V_b) as a function of gap distance (d) for pressures (p) of 3 kPa, 50 kPa, and 101 kPa.

100 GHz^{30–32}. Additionally, electric field distribution plays a critical role in low-pressure gas breakdown^{33,34}. While most vacuum electronics studies focus on device failures due to space-charge limited emission^{35–38} and multipactor^{39–41}, vacuum breakdown has also been examined²⁸. The development of carbon nanotube systems for vacuum electron emission^{42–44} and the potential for nanoscale systems at higher pressures⁴⁵ motivates additional characterization of electron emission experimentally at subatmospheric pressure. While some studies have assessed pressure on the order of a few torr²¹, a study detailing the impact of pressure on the intersection of the combined FE/TA breakdown regime with PL has not been performed. This letter measures breakdown voltage at microscale for several subatmospheric pressures and assesses this behavior using a universal, matched asymptotic solution²⁶. As we shall show, this universal model gives the conditions under which FE and TA driven breakdown transition to PL to the left of the Paschen minimum, yielding the appearance of an extended plateau.

Results

Experimental description and results. A detailed description and block diagram of the experimental setup can be found in ref.²⁷. Briefly, the experimental system consists of a nanosecond pulse generation unit, a synchronous and delay triggering unit, an *in-situ* optical imaging unit, and an electrical parameter measurement unit. We generated the nanosecond pulse by feeding DC voltage into a high voltage solid-state switch (BEHLKE HTS-50-08-UF), which delivered adjustable nanosecond pulses with a maximum amplitude up to 5 kV. Synchronous triggering was performed by a function generator (RIGOL DG3101A). We integrated an *in-situ* optical imaging unit with an optical microscope to achieve micron-scale spatial resolution and a high-speed gated ICCD camera to attain nanosecond-scale temporal resolution. A metallographic microscope (OLYMPUS BX51M) with a long work distance objective lens ($50\times$) magnified the micron-scale test specimen. We used a high-speed gated ICCD camera (ANDOR iStar 334 T) to detect light emission during gas breakdown with a minimum gate width of 2 ns. A current coil (Pearson 6585) monitored pulse current, an attenuator probe (100:1) measured pulsed voltage, and a digital oscilloscope (LeCroy 104MXs-B) reported the signal. This letter focuses on breakdown measurements; further experimental assessments will be reported elsewhere.

Figure 1 shows the experimental results for breakdown voltage in air at pressures of 3, 50, and 101 kPa for gap distances from 1–25 μm . When plotted as a function of d , V_b is relatively insensitive to p at smaller gap distances where one anticipates field emission driven breakdown. Measured V_b diverges with p for $d \gtrsim 5 \mu\text{m}$. While our previous theoretical studies have examined V_b as a function of either p or d ^{24–26}, the relatively large difference in p here suggests that collisionality, or pd , may elucidate the experimental behavior. Thus, we will assess $V_b(pd)$ when we apply the matched asymptotic theory to the experimental data.

Theoretical analysis and results. We start from the general, nondimensional, universal (true for any gas) breakdown equation, given by²⁶

$$\frac{\exp[\bar{\phi}^{3/2}/(\beta\bar{E})]}{\beta\bar{\phi}^{1/2}\exp(\bar{\phi}^{-1/2})}\sqrt{\frac{\bar{T}\bar{E}}{\bar{p}\bar{d}^2}}\frac{\{1 - \gamma_{SE}[\exp(\bar{\alpha}\bar{d}) - 1]\}}{\exp(\bar{\alpha}\bar{d}) - 1} = \exp(1)(1 + 2\bar{E}), \quad (1)$$

where $\bar{\phi} = \phi/\phi_*$ is the dimensionless work function of the electrode material with $\phi_* = [(3.79 \times 10^{-4})^2 B_{FN}]^2$ in eV, β is the field enhancement factor, $\bar{E} = E/E_*$ is the dimensionless breakdown electric field with $E_* = 0.95 B_{FN} \phi_*^{3/2}$ in V/m, $\bar{p} = p/p_*$ is the dimensionless pressure with $p_* = E_* B_p^{-1}$ in Torr, $\bar{d} = d/L$ is the dimensionless gap distance with $L = p_*^{-1} A_p^{-1}$ in m, $\bar{T} = T/T_*$ is the dimensionless temperature with $T_* = [(\pi m \sigma_{CE} B_p)/(8ek)]\{A_{FN}/[\varepsilon_0 A_p t^2(y)\phi_*]\}^2$ in K, γ_{SE} is the secondary emission coefficient, $\bar{\alpha} = \alpha L$ is the dimensionless ionization coefficient with $\alpha = A_p p \exp(-B_p p/E)$ in m^{-1} , and all terms without bars correspond to the dimensional (measured) quantities of those with bars. Additionally, A_{FN} and B_{FN} are Fowler-Nordheim constants, A_p and B_p are gas constants, m is the mass of the gas atom in kg, σ_{CE} is the charge exchange cross section, e

Parameter	Name	Value	Unit
V_B	Breakdown voltage	Variable	V
V_*	Breakdown voltage scale	24.3	V
d	Gap distance	Variable	m
L	Gap distance scale	3.92×10^{-12}	m
E	Breakdown electric field	Variable	V/m
E_*	Breakdown electric field scale	6.20×10^{12}	V/m
p	Pressure	Variable	kPa
p_*	Pressure scale	1.70×10^8	Torr
T	Temperature	300	K
T_*	Temperature scale	7976	K
ϕ	Work function	4.7	eV
ϕ_*	Work function scale	96.81	eV
β	Field enhancement factor	Variable	N/A
γ_{SE}	Secondary emission coefficient	10^{-5}	N/A

Table 1. Summary of parameters considered in this work.

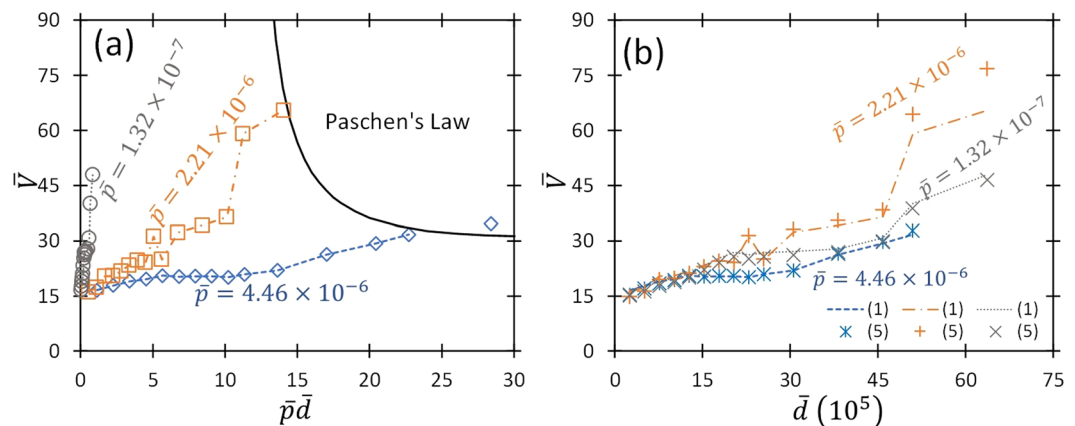


Figure 2. (a) Dimensionless breakdown voltage, \bar{V} , as a function of the product of dimensionless pressure and gap distance, $\bar{p}\bar{d}$, for various pressures compared to results from the universal Paschen's law (UPL) determined from (2) with $\gamma_{SE} = 10^{-5}$ using β from Fig. 3. The symbols represent experimental data points and the dashed lines represent the numerical solution of (1), using field enhancement factor β as a fitting parameter. (b) Dimensionless breakdown voltage, \bar{V} , as a function of dimensionless gap distance, \bar{d} . Numerical results from (1) are shown as the dashed lines and the limiting results of equation (5) are shown as symbols with $\gamma_{SE} = 10^{-5}$ using β from Fig. 3. There is an average percent difference between equations (1) and (5) of 3.71%.

is the electron charge, k is Boltzmann's constant, ϵ_0 is the permittivity of free space, and $t^2(y) \approx 1.1^{46}$ is a Fowler-Nordheim correction factor used since the Schottky reduction factor, y , is sufficiently less than one for the data considered here. Table 1 summarizes typical values.

We numerically solve Equation (1) and choose β to fit to the nondimensionalized experimental data from Fig. 1 as a function of $\bar{p}\bar{d}$, with $\gamma_{SE} = 10^{-5}$ and $\bar{V} = E\bar{d}$. Figure 2a shows the fitting of Equation (1) and the universal PL (UPL)²⁶, given by

$$\bar{V}_B = \frac{\bar{p}\bar{d}}{\ln(\bar{p}\bar{d}) - \ln[\ln(1 + \gamma_{SE}^{-1})]}, \quad (2)$$

to the measured data with β shown in Fig. 3. We note that the experimental data for 50 kPa and 101 kPa actually intersects with the UPL, indicating the transition from the combined FE/TA regime to the traditional PL. Moreover, the 50 kPa data intersects the UPL to the left of the Paschen minimum, while the 101 kPa data intersects the UPL near the minimum, as observed in previous applications of this theory to atmospheric pressure data^{26,27}. This stands to reason since previous results⁴⁷ indicate the transition should occur around 18 μm . Since the curves in Fig. 2a are universal, they hold for any combination of parameters that yield these intersections, so the intersection with the UPL could occur on either side of the minimum at atmospheric pressure depending upon gas and electrode conditions.

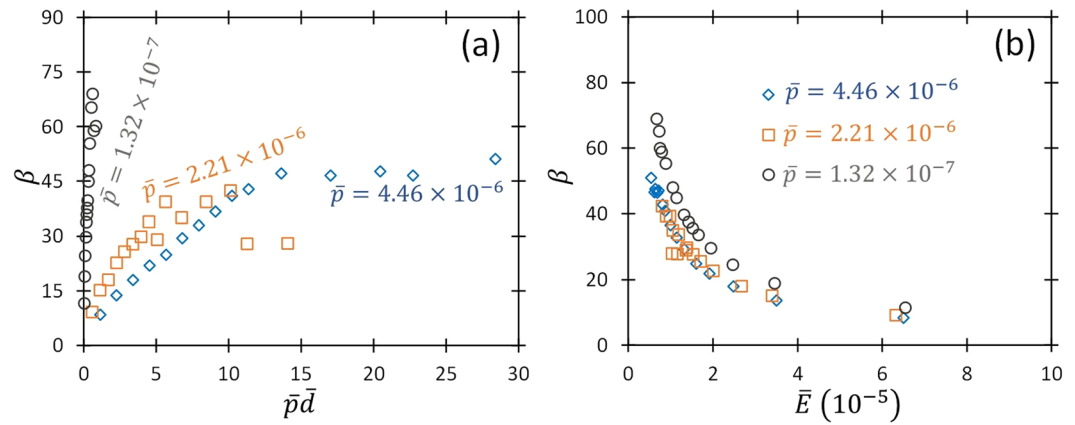


Figure 3. (a) Field enhancement factor, β , as a function of the product of the dimensionless pressure and gap distance, $\bar{p}\bar{d}$, obtained by fitting the experimental data from Fig. 2. (b) Field enhancement factor, β , as a function of the dimensionless electric field, \bar{E} .

We can analytically assess this intersection since $\bar{\alpha}\bar{d} \gg 1$ generally for the data considered here, allowing us to simplify \bar{V} to obtain²⁶

$$\bar{V} = \frac{\bar{d}}{\Lambda_2} \left[-\Delta_2 - \sqrt{\Delta_2^2 - 2\Lambda_2(\bar{\phi}^{3/2}/\beta)} \right], \quad (3)$$

where

$$\Delta_2 = \frac{\ln[\bar{T}\bar{p}^{-1}\bar{d}^{-2}]}{2} - \ln[\beta\bar{\phi}^{1/2}] - \bar{\phi}^{-1/2} - \frac{\ln[\Lambda_2]}{2} - \ln \left[\exp \left(\frac{\bar{p}\bar{d}}{\exp(1)} \right) - 1 \right] + \ln \left[1 - \gamma_{SE} \left[\exp \left(\frac{\bar{p}\bar{d}}{\exp(1)} \right) \right] \right] - \frac{3}{2}, \quad (4)$$

and $\Lambda_2 = 1 \times 10^5$. Analogous to ref.²⁷, we can further simplify (3) to obtain a limiting equation for \bar{V} , given by

$$\bar{V} = \frac{\bar{\phi}^{3/2}}{\beta|\Delta_2|} \bar{d}. \quad (5)$$

Figure 2b compares the limiting results from equation (5) to the numerical calculations from equation (1) using β from Fig. 3. The limiting results agree well with equation (1) at low $\bar{p}\bar{d}$ and deviate as $\bar{p}\bar{d}$ increases. The numerical results of equation (1) and analytic results of equation (3) have an average percent difference of 3.97% while the results of equation (1) and the limiting results of equation (5) differ by an average of 3.71%. Thus, we use equation (5) in Fig. 2b and the remainder of the analytic assessment without sacrificing accuracy. Also important concerning global universality, Fig. 2 emphasizes that the breakdown voltage scales differently in the different regimes. Upon satisfying the PL condition (transitioned from the FE/TA combined regime to the conventional PL regime), the behavior the breakdown voltage scales with pd and one recovers the UPL. At smaller gaps, Fig. 2a shows that breakdown voltage scales with d . Thus, while breakdown exhibits universal behavior, the scaling of this universal behavior varies depending upon the dominant breakdown mechanism.

Figure 3 shows β for fitting equation (1) to the data in Fig. 2 as functions of the product of dimensionless pressure and gap distance, $\bar{p}\bar{d}$, and the dimensionless electric field, \bar{E} . For 50 kPa and 101 kPa, β increases linearly with increasing $\bar{p}\bar{d}$, as observed previously in the FE dominant regime at atmospheric pressure^{26,27}. Eventually, β approaches a constant, which corresponds to the transition from the FE to TA regimes, as also observed previously^{26,27}. Interestingly, this occurs at a lower $\bar{p}\bar{d}$ for 50 kPa. Previous results indicate that this transition is not solely driven by $\bar{p}\bar{d}$, but by \bar{p} and \bar{d} independently, which is supported by this work. For 3 kPa, β also increases linearly at low $\bar{p}\bar{d}$, but much more rapidly. While the current experiments cannot achieve sufficient voltage to measure V_B at larger d for 3 kPa, the theory suggests that the intersection with the UPL will occur at a much higher β than either of the other pressures studied. Figure 3b indicates that β is a function of \bar{E} , which is also supported by previous work^{48,49}. Interestingly, β at the two highest pressures studied here is identical when plotted as a function of \bar{E} , suggesting potential universality in this regime. Future work at lower pressures and larger gap distances can better characterize these transitions and further characterize the dependence of β on \bar{E} .

Finally, we consider the impact of γ_{SE} , β , and $\bar{\phi}$, on the transition from the FE/TA regime to the UPL. Understanding how these parameters affect breakdown is vital for developing a predictive model, since γ_{SE} and β are difficult to determine *a priori* and the asymptotic prediction of V_B is very sensitive to variations in β and $\bar{\phi}$ in the FE/TA regime⁵⁰. Thus, elucidating the influence of these terms on V_B will clarify the transition to UPL under

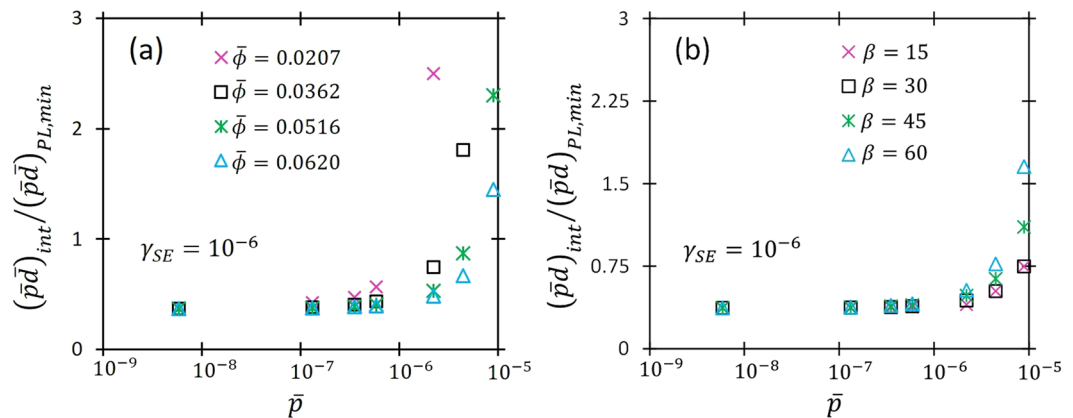


Figure 4. The ratio of the product of dimensionless pressure and gap distance, $\bar{p}\bar{d}$, causing the transition to Paschen's law, $(\bar{p}\bar{d})_{int}$, to $\bar{p}\bar{d}$ corresponding to the Paschen minimum, $(\bar{p}\bar{d})_{PL,min}$, as a function of \bar{p} for various values of (a) $\bar{\phi}$ with $\beta=60$ and $\gamma_{SE}=10^{-6}$, and (b) β with $\gamma_{SE}=10^{-6}$ and $\bar{\phi}=0.0465$.

different p and d . The transition from the FE/TA regime to the UPL occurs when the limiting expression of equation (5) matches the UPL from equation (2), so we numerically solve

$$\frac{\bar{p}\beta|\Delta_2|}{\bar{\phi}^{3/2}\{\ln(\bar{p}\bar{d}) - \ln[\ln(1 + \gamma_{SE}^{-1})]\}} = 1 \quad (6)$$

for \bar{d} with a given γ_{SE} , β , and \bar{p} . Figure 4 shows the ratio of $\bar{p}\bar{d}$ for the transition, $(\bar{p}\bar{d})_{int}$, to the value corresponding to the standard "Paschen minimum" of Equation (2) by setting $d\bar{V}/d(\bar{p}\bar{d}) = 0$ to give

$$(\bar{p}\bar{d})_{PL,min} = \exp\{1 + \ln[\ln(1 + \gamma_{SE}^{-1})]\}. \quad (7)$$

When $(\bar{p}\bar{d})_{int}/(\bar{p}\bar{d})_{PL,min} < (>)1$, Equations (2) and (3) intersect to the left (right) of the traditional Paschen minimum. For example, at atmospheric pressure, $\beta=60$, $\phi=4.7$ eV, and $\gamma_{SE}=10^{-4}$ the FE/TA model and the UPL intersect to the left of the Paschen minimum. However, reducing ϕ to 3 eV shifts the intersection to the right of the Paschen minimum. Figure 4a shows $(\bar{p}\bar{d})_{int}/(\bar{p}\bar{d})_{PL,min}$ as a function of \bar{p} for $\beta=60$ and $\gamma_{SE}=10^{-6}$ considering $\phi=2, 3.5, 5$, and 6 eV ($\bar{\phi}=0.0207, 0.0362, 0.0516$, and 0.0620) and Fig. 4b shows $(\bar{p}\bar{d})_{int}/(\bar{p}\bar{d})_{PL,min}$ as a function of \bar{p} for various β at $\gamma_{SE}=10^{-6}$. We note that ϕ does not have a significant effect on the transition point until $\bar{p} \approx 2 \times 10^{-6}$ (which corresponds to 380 Torr). We also observe the same behavior for any small value of γ_{SE} , such as $\gamma_{SE}=10^{-6}$. This is analogous to previous observations that γ_{SE} does not play a vital role until TA dominates breakdown (often occurring somewhere around atmospheric pressure)^{26,50}. Figure 4b indicates that increasing β from 15 to 60 does not influence the transition point until $\bar{p} \approx 5 \times 10^{-6}$ (950 Torr). Reducing ϕ can shift the transition to the left of the PL minimum at subatmospheric pressures, but changing β does not shift the transition to the left of the minimum until the pressure exceeds atmospheric pressure. Varying γ_{SE} yielded similar behavior on the intersection with PL as changing β .

Conclusion

In summary, we applied a gas breakdown theory^{26,27} to assess experimental results for breakdown voltage at various pressures. Using β as a fitting parameter, we achieved excellent agreement between the exact numerical solution of the theory and the experimental results, and demonstrated that the analytic model differed from experiment by an average of 3.71%. We showed that experimental conditions, particularly electrode work function, can drive the intersection between the coupled FE/TA model and the UPL to the left or the right of the traditional Paschen minimum, providing a potential contributing factor determining whether V_B decreases with decreasing pd or an extended plateau occurs. Furthermore, the results showed that β and γ_{SE} have little influence on the location of the transition below atmospheric pressure, but ϕ has a greater influence. Future studies quantifying the change in work function⁵¹ with multiple breakdown events will further elucidate how breakdown behavior changes with constant gap distance. For example, one can envision an initial work function leading to a transition to the UPL to the right of the minimum, with subsequent breakdown events occurring to the left after electrode surface damage potentially decreases work function if it enhances surface roughness⁵¹. Future work quantifying how changes in work function due to surface roughness or chemical roughness⁵² effect the system and incorporating thermionic emission⁵³ into the model will enhance the utility and completeness of the model across multiple operating regimes. A more thorough understanding of this behavior is vital to accurately predict breakdown behavior and electron emission overall.

References

- Ju, Y. & Sun, W. Plasma assisted combustion: Dynamics and chemistry. *Prog. Energy and Comb. Sci.* **48**, 21–83 (2015).
- Martinez-Sanchez, M. & Pollard, J. E. Spacecraft electric propulsion—An overview. *J. Propul. Power* **14**, 688–699 (1998).
- Becker, K. H., Schoenbach, K. H. & Eden, J. G. Microplasmas and applications. *J. Phys. D: Appl. Phys.* **39**, R55–R70 (2006).

4. Schoenbach, K. H. & Becker, K. 20 years of microplasma research: a status report. *Eur. Phys. J. D* **70**, 29 (2016).
5. Becker, K. *et al.* Environmental and biological applications of microplasmas. *Plasma Phys. Control. Fusion* **47**, B513–B523 (2005).
6. Kong, M. *et al.* Plasma medicine: an introductory review. *New J. Phys.* **11**, 115012 (2009).
7. Laroussi, M. Low-temperature plasma jet for biomedical applications: a review. *IEEE Trans. Plasma Sci.* **43**, 703712 (2015).
8. Rezvykh, K. A. & Romanov, V. A. Gases breakdown voltage calculation for the case of accelerator nonuniform fields by the method of base. *Nuc. Instrum. Meth. Phys. Res. A* **423**, 203–212 (1999).
9. Welch, D. R., Cuneo, M. E., Olson, C. L. & Mehlhorn, T. A. Gas breakdown effects in the generation and transport of light ion beams for fusion. *Phys. Plasmas* **3**, 2113–2121 (1996).
10. Bogue, R. MEMS sensors: Past, present, and future. *Sens. Rev.* **27**, 7–13 (2007).
11. Craighead, H. Nanoelectromechanical systems. *Science* **290**, 1532–1535 (2000).
12. Garner, A. L. *et al.* Experimental validation of a compact, flexible pulsed power architecture for *ex vivo* platelet activation. *PLoS ONE* **12**, e0181214 (2017).
13. Paschen, F. Ueber die zum Funkenübergang in Luft, Wasserstoff und Kohlensäure bei verschiedenen Drucken erforderliche Potentialdifferenz. *Ann. Phys.* **273**, 69–96 (1889).
14. Boyle, W. S. & Kisliuk, P. Departure from Paschen's law of breakdown in gases. *Phys. Rev.* **97**, 255–259 (1955).
15. Go, D. B. & Venkatraman, A. Microscale gas breakdown: ion-enhanced field emission and the modified Paschen's curve. *J. Phys. D* **47**, 503001 (2014).
16. Venkatraman, A. & Alexeenko, A. A. Scaling law for direct current field emission-driven microscale gas breakdown. *Phys. Plasmas* **19**, 123515 (2012).
17. Semnani, A., Venkatraman, A., Alexeenko, A. & Peroulis, D. Frequency response of atmospheric pressure gas breakdown in micro/nanogaps. *Appl. Phys. Lett.* **103**, 063102 (2013).
18. Radmilović-Radjenović, M. & Radjenović, B. An analytical relation describing the dramatic resuction of the breakdown voltage for the microgap devices. *Europhys. Lett.* **83**, 25001 (2008).
19. Go, D. B. & Pohlman, D. A. A mathematical model of the modified Paschen's curve for breakdown in microscale gaps. *J. Appl. Phys.* **107**, 103303 (2010).
20. Tirumala, R. T. & Go, D. B. An analytical formulation for the modified Paschen's curve. *Appl. Phys. Lett.* **97**, 151502 (2010).
21. Torres, J. M. & Dhariwal, R. S. Electric field breakdown at micrometer separations. *Nanotechnology* **10**, 102–107 (1999).
22. Chen, C. H., Yeh, J. A. & Wang, P. J. Electrical breakdown phenomena for devices with micron separations. *J. Micromech. Microeng.* **16**, 1366–1373 (2006).
23. Radmilović-Radjenović, M., Radjenović, B., Matejčik, S. & Klas, M. The breakdown phenomena in micrometer scale direct-current gas discharges. *Plasma Chem. Plasma Process.* **34**, 55–64 (2014).
24. Loveless, A. M. & Garner, A. L. Scaling laws for gas breakdown for nanoscale to microscale gaps at atmospheric pressure. *Appl. Phys. Lett.* **108**, 234103 (2016).
25. Loveless, A. M. & Garner, A. L. Generalization of microdischarge scaling laws for all gases at atmospheric pressure. *IEEE Trans. Plasma Sci.* **45**, 574–583 (2017).
26. Loveless, A. M. & Garner, A. L. A universal theory for gas breakdown from microscale to the classical Paschen law. *Phys. Plasmas* **24**, 113522 (2017).
27. Meng, G. *et al.* Demonstration of field emission driven microscale gas breakdown for pulsed voltages using *in-situ* optical imaging. *Phys. Plasmas* **25**, 082116 (2018).
28. Little, R. P. & Smith, S. T. Electrical breakdown in vacuum. *IEEE Trans. Electron Dev.* **12**, 77–83 (1965).
29. Fu, Y., Krek, J., Zhang, P. & Verboncoeur, J. P. Gas breakdown in microgaps with a surface protrusion on the electrode. *IEEE Trans. Plasma Sci.*, in press, <https://doi.org/10.1109/TPS.2018.2878011>.
30. Booske, J. H. Plasma physics and related challenges of millimeter-wave-to-terahertz and high power microwave generation. *Phys. Plasmas* **15**, 055502 (2008).
31. Neuber, A. A., Krile, J. T., Edmiston, G. F. & Krompholz, H. G. Dielectric surface flashover at atmospheric conditions under high-power microwave excitation. *Phys. Plasmas* **14**, 057102 (2007).
32. Braun, H. H., Döbert, S., Wilson, I. & Wuensch, W. Frequency and temperature dependence of electrical breakdown at 21, 30, and 39 GHz. *Phys. Rev. Lett.* **90**, 224801 (2003).
33. Fu, Y., Yang, S., Zou, X., Luo, H. & Wang, X. Effect of distribution of electric field on low-pressure gas breakdown. *Phys. Plasmas* **24**, 023508 (2017).
34. Fu, Y., Krek, J., Zhang, P. & Verboncoeur, J. P. Evaluating microgap breakdown mode transition with electric field non-uniformity. *Plasma Sources Sci. Technol.* **27**, 095014 (2018).
35. Child, C. D. Discharge from hot CaO. *Phys. Rev. (Series I)* **32**, 492–511 (1911).
36. Langmuir, I. The effect of space charge and residual gases on thermionic currents in high vacuum. *Phys. Rev.* **2**, 450–486 (1913).
37. Benilov, M. S. The Child-Langmuir law and analytical theory of collisionless to collision-dominated sheaths. *Plasma Sources Sci. Technol.* **18**, 014005 (2009).
38. Lau, Y. Y., Liu, Y. & Parker, R. K. Electron emission: From the Fowler-Nordheim relation to the Child-Langmuir law. *Phys. Plasmas* **1**, 2082–2085 (1994).
39. Kishek, R. A., Lau, Y. Y., Ang, L. K., Valfells, A. & Gilgenbach, R. M. Multipactor discharge on metals and dielectrics: Historical review and recent theories. *Phys. Plasmas* **5**, 2120–2126 (1998).
40. Gopinath, V. P., Verboncoeur, J. P. & Birdsall, C. K. Multipactor electron discharge physics using an improved secondary emission model. *Phys. Plasmas* **5**, 1535–1540 (1998).
41. Kishek, R. A. Ping-pong modes and higher-periodicity multipactor. *Phys. Plasmas* **20**, 056702 (2013).
42. She, J. C., Xu, N. S., Deng, S. Z. & Chen, J. Vacuum breakdown of carbon-nanotube field emitters on a silicon tip. *Appl. Phys. Lett.* **83**, 2671–2673 (2003).
43. Descoeudres, A., Levinsen, Y., Calatroni, S., Taborrelli, M. & Wuensch, W. Investigation of the dc vacuum breakdown mechanism. *Phys. Rev. Accel. Beams* **12**, 092001 (2009).
44. Collins, P. G., Hersam, M., Arnold, M., Martel, R. & Avouris, P. Current saturation and electrical breakdown in multiwalled carbon nanotubes. *Phys. Rev. Lett.* **86**, 3128–3131 (2001).
45. Li, M., Tang, H. X. & Roukes, M. L. Ultra-sensitive NEMS-based cantilevers for sensing, scanned probe and very high-frequency application. *Nature Nanotech.* **2**, 114–120 (2007).
46. Spindt, C. A., Brodie, I., Humphrey, L. & Westerberg, E. R. Physical properties of thin-film field emission cathodes with molybdenum cones. *J. Appl. Phys.* **47**, 5248–5263 (1976).
47. Meng, G. *et al.* Spatio-temporal dynamics of pulsed gas breakdown in microgaps. *Phys. Plasmas* **26**, 014506 (2019).
48. Venkatraman, A. Electric field enhancement due to a saw-tooth asperity in a channel and implications on microscale gas breakdown. *J. Phys. D: Appl. Phys.* **47**, 425205 (2014).
49. Buendia, J. A. & Venkatraman, A. Field enhancement factor dependence on electric field and implications on microscale gas breakdown: Theory and experimental interpretation. *Europhys. Lett.* **112**, 55002 (2015).
50. Dynako, S. D., Loveless, A. M. & Garner, A. L. Sensitivity of modeled microscale gas breakdown voltage due to parametric variation. *Phys. Plasmas* **25**, 103505 (2018).
51. Li, W. & Li, D. Y. On the correlation between surface roughness and work function in copper. *J. Chem. Phys.* **122**, 064708 (2005).

52. Kim, K. S., Hurtado, J. A. & Tan, H. Evolution of a surface-roughness spectrum caused by stress in nanometer-scale chemical etching. *Phys. Rev. Lett.* **83**, 3872–3875 (1999).
53. Jensen, K. L. A tutorial on electron sources. *IEEE Trans. Plasma Sci.* **46**, 1881–1899 (2018).

Acknowledgements

This work was supported by the Office of Naval Research (Grant No. N00014-17-1-2702), the National Natural Science Foundation of China (Grant No. 51607138, 51521065), China Postdoctoral Science Foundation (Grant No. 2016M602820), Research Foundation of State Key Laboratory of Intense Pulsed Radiation Simulation and Effect (Grant No. SKLIPR.1512). A. M. L. also gratefully acknowledges funding from a graduate scholarship from the Directed Energy Professional Society.

Author Contributions

A.M.L., G.M. and A.L.G. designed the study. A.M.L. and A.L.G. conceived the theory and A.M.L. carried out the theoretical calculations. Y.C. and G.M. conceived and planned the experiment. Q.Y., F.W. and K.W. performed the experiment. A.M.L., G.M. and A.L.G. interpreted the results and wrote the manuscript. All authors reviewed and approved the manuscript

Additional Information

Competing Interests: The authors declare no competing interests.

Publisher's note: Springer Nature remains neutral with regard to jurisdictional claims in published maps and institutional affiliations.



Open Access This article is licensed under a Creative Commons Attribution 4.0 International License, which permits use, sharing, adaptation, distribution and reproduction in any medium or format, as long as you give appropriate credit to the original author(s) and the source, provide a link to the Creative Commons license, and indicate if changes were made. The images or other third party material in this article are included in the article's Creative Commons license, unless indicated otherwise in a credit line to the material. If material is not included in the article's Creative Commons license and your intended use is not permitted by statutory regulation or exceeds the permitted use, you will need to obtain permission directly from the copyright holder. To view a copy of this license, visit <http://creativecommons.org/licenses/by/4.0/>.

© The Author(s) 2019